Electrical Leakage Current Evolution in Photovoltaic Modules: A Reduced-Order Simulation of Coupled Ionic Conduction and Interface Degradation

Ali Kareem Jabbar[a], Zainab Hussein Abbas[b], Muna Mahmood Badan[c], Hassanein Riyadh Mahmood[d,1,*]

[a] *Department of Cyber Security, College of Computer Science and Information Technology, Wasit University, Iraq*
[b] *Department of Electrical Engineering, College of Engineering, Wasit University, Iraq*
[c] *Department of Physics, College of Education for Pure Science, Wasit University, Iraq*
[d] *Department of Renewable Energy Techniques, Technical Institute-Kut, Middle Technical University, Baghdad, Iraq*
[1] *hassanein-riyadh@mtu.edu.iq**
* *corresponding author*

ARTICLE INFO

Article history
Received Mar 27, 2026
Received Apr 2, 2026
Revised May 15, 2026
Accepted Jun 19, 2026

Keywords
photovoltaic module reliability
leakage current
encapsulant delamination
damp heat
ionic transport
potential-induced degradation

ABSTRACT

Leakage current in photovoltaic (PV) modules is usually read as a passive measure of encapsulant conductivity, although its paths cross interfaces that degrade mechanically and chemically. This computational study determines when and under which accelerated-test loading the leakage path hands over from the encapsulant bulk to debonded interfaces. A reduced-order model was formulated in which interface debonding is the explicit two-way coupling variable: moisture ingress, thermo-viscoelastic mismatch stress and hydrolytic loss of adhesion drive a cohesive damage law; damaged interfaces become thin interphase conduits in parallel with the bulk, glass and condensate-film paths; and faradaic charge at the frame contact (Butler–Volmer kinetics, 1000 V bias) feeds back into damage. Damp-heat (DH), thermal-cycling (TC) and humidity-freeze (HF) tests of EVA and POE mini-modules were simulated with four nested models and uncalibrated, representative parameters. Under DH, the predicted current accelerated only after encapsulant saturation, rising almost threefold after 400 h as hydrolytic weakening let a debond front advance from the frame; moisture-dependent conductivity alone could not reproduce this stage. The bulk-to-interface handover occurred after about 426 h under DH and within the first HF cycle (21.8 h), whereas dry TC damaged the edge with little change in current. POE suppressed the mechanism under DH and delayed it under HF. Within the explored parameter range, the handover time followed a temperature–humidity acceleration law and was governed mainly by the adhesion-hydrolysis rate. Subject to experimental validation, it is proposed as a mechanism-based metric for encapsulant selection and multi-stress test design.

I. Introduction

Leakage current flows in photovoltaic (PV) modules between the cell circuit and the grounded frame, and system voltages reach 1000–1500 V. The current is a precursor of potential-induced degradation (PID), metallization corrosion and power loss (del Cueto & McMahon, 2002; Luo et al., 2017; Yamaguchi et al., 2021). It follows several parallel paths: through the encapsulant bulk, through the glass, along the glass surface and across the laminate edge. Their contributions change with temperature, humidity and surface wetness (del Cueto & McMahon, 2002; Dhere et al., 2014a, 2014b). Ions carry the current in the polymer and glass, and electrons carry it in the metal, so electrochemical reactions occur wherever the carrier changes (Kempe et al., 2023). Leakage current, in turn, accelerates delamination and corrosion (Li et al., 2018). The problem matters at fleet scale. Crystalline-silicon modules accounted for about 95% of the PV market in 2020 (Ballif et al., 2022); a compendium of more than 11,000 field degradation rates reported median losses of 0.5–0.6% per year for crystalline-silicon modules, with higher rates in hot climates for some products (Jordan et al., 2016), and a recent fifteen-year forensic study of polycrystalline modules found 2.56% per year, with delamination attributed to moisture, oxygen and light exposure (Tsanakas et al., 2026). New cell and encapsulant combinations have, in addition, introduced damp-heat failure modes that depend strongly on the encapsulation bill of materials (Fu et al., 2026; Sen et al., 2024; Wang et al., 2026).

Moisture drives most of this evolution. Water enters the encapsulant through a breathable backsheet and the laminate edge (Blom et al., 2025; Kempe, 2006; Mitterhofer et al., 2024; Segbefia et al., 2021). It raises ionic mobility and hydrolyses the acetate groups of EVA into acetic acid (Semba, 2020). It also weakens interfacial adhesion

through viscoelastic and hydrolytic mechanisms (Bosco et al., 2019; K. Liu et al., 2024; Novoa et al., 2016; Spinella et al., 2022). These studies quantify moisture ingress and adhesion loss convincingly, but they treat the electrical response as a separate outcome; the consequence of adhesion loss for the leakage current is therefore inferred rather than computed.

A. Research Gap and Novel Contributions

Two modelling traditions address this problem, but separately. Hygro-thermo-mechanical models with cohesive interfaces predict where PV laminates delaminate (Z. Liu et al., 2022). Field and Poisson–Nernst–Planck models predict leakage current and Na^+ transport for a fixed material state (Martinez-Loran et al., 2022; van Soestbergen et al., 2008). Coupled damage–moisture theories exist for polymer composites (Weitsman, 1987), but have not been applied to leakage current. Three gaps follow:

- No attribution of a rising current. An accelerated test cannot tell whether a rising leakage current comes from moisture uptake in the bulk or from an opening interfacial conduit, although the two have different implications for field reliability.
- Damage without electrical consequence. Delamination models do not compute how debonding changes the leakage paths.
- Conductivity without mechanical state. Leakage models treat conductivity as a function of temperature and moisture only.

The objective of this study is to determine, by simulation, whether, when and under which accelerated-test loading the leakage path of a framed PV laminate hands over from the encapsulant bulk to debonded interfaces. This paper addresses these gaps with four contributions:

- Two-way coupling through interface damage. Hygrothermal stress and hydrolytic weakening drive cohesive damage. The damage opens thin interphase conduits in parallel with the bulk paths, and the faradaic charge at the frame contact feeds back into the damage.
- A bounded electrochemical closure. Almost the entire bias drops across the resistive laminate, so the Butler–Volmer overpotential stays within its physical range.
- A dimensional and thermodynamic consistency check of the complete constitutive set, including the damage-amplified conduction and the corrosion feedback (Section II.A.7 and Appendix A).
- Mechanism-resolving virtual tests. DH, TC and HF simulations of EVA and POE laminates with four nested models, a variance-based sensitivity analysis and a temperature–humidity map identify when, where and under which loading the leakage path hands over from the bulk to the interface. The resulting handover time is proposed as a candidate durability metric, subject to experimental validation.

II. Method

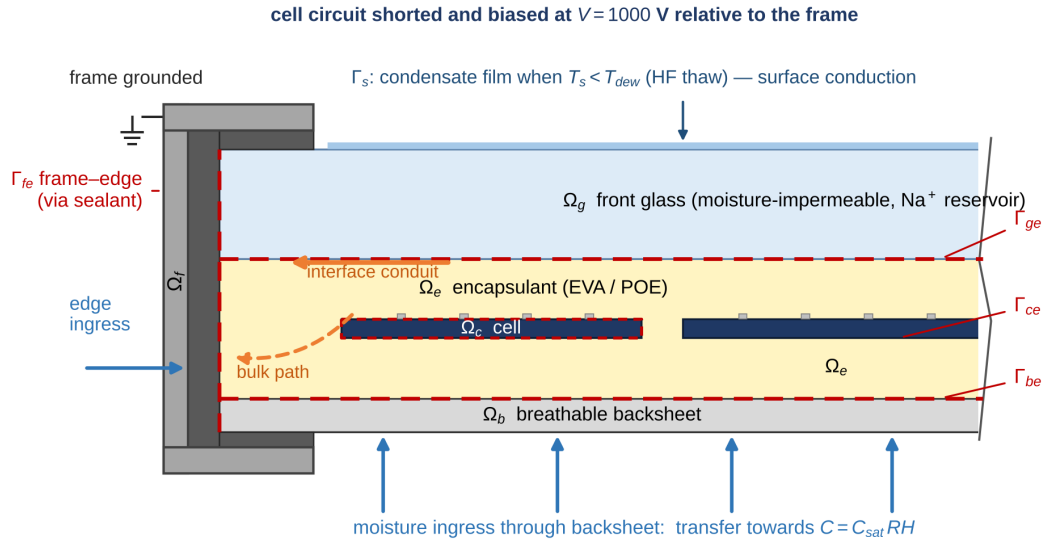
A. Model Formulation

1) Domain and Reduced-Order Setting

The analysis considers the edge region of a framed glass/encapsulant/cell/encapsulant/backsheet laminate (Fig. 1). The lateral coordinate x runs from the frame ($x = 0$) towards the module centre. The cells begin at $x_c = 10$ mm, and the domain extends to $L = 30$ mm, where a symmetry condition applies. The lateral distances (≈10 mm) exceed the layer thicknesses ($h_e = 0.9$ mm of encapsulant in total and $h_g = 3.2$ mm of glass) by an order of magnitude, so each field is averaged through the thickness and resolved along x. The material interfaces Γ_I (glass–, cell– and backsheet–encapsulant and frame edge; Γ_{ge}, Γ_{ce}, Γ_{be} and Γ_{fe} in Fig. 1) enter as through-thickness properties:

- The frame-edge and glass–encapsulant interfaces, which debond first, are represented by a single cohesive damage variable $d(x,t)$;
- after debonding, the interface carries a thin interphase of thickness $h_I = 20$ μm that conducts ions along x.

The module perimeter $P = 2.4$ m (600 × 600 mm^2 mini-module) converts per-unit-length quantities into terminal values.



Schematic, not to scale. Each Γ_i carries a cohesive law and a thin interphase of thickness h_i whose conductance is amplified by $(1+\alpha_d d)$.

Fig. 1. Edge region of the framed laminate, interfaces and boundary conditions. Moisture enters through the breathable backsheet and the edge sealant. The glass is impermeable to moisture but is an Na^+ reservoir. The cell circuit is biased at 1000 V relative to the grounded frame, and condensation on the glass (Γ_s) opens a surface path during humidity-freeze thaws. Orange arrows indicate the bulk and interface leakage paths.

2) Moisture Transport

The normalised water content $C(x,t)$ (volume fraction of absorbed water) obeys

$$\frac{\partial C}{\partial t} = \frac{\partial}{\partial x}\left(D\,\frac{\partial C}{\partial x}\right) + \frac{k_b}{h_e}(C_{sat}\,RH - C) \tag{1}$$

$$D = D_{85}\,\mathcal{A}(E_D,T)[1+\beta_c a_w^2], \qquad C_{sat} = C_{s,85}\,\mathcal{A}(E_s,T), \qquad a_w = C/C_{sat} \tag{2}$$

where $\mathcal{A}(E,T) = \exp\left[-E/R_g\,(1/T - 1/T_r)\right]$ is a dimensionless Arrhenius factor referred to $T_r = 358.15$ K (85 °C), so that $\mathcal{A}(E,T_r) = 1$ and, for $E > 0$, $\mathcal{A}$ increases with T. a_w is the water activity, D is in $m^2\ s^{-1}$ and the last term of Eq. (1), in s^{-1}, is ingress through the backsheet with transfer coefficient k_b (m s^{-1}). With $E_s > 0$, the solubility C_{sat} increases with temperature, as reported for EVA (Kempe, 2006). At the edge, the sealant admits a flux $-D\ \partial C/\partial x = k_s(C_{sat}RH - C)$ with k_s in m s^{-1}; k_b and k_s share the activation energy E_b. At $x = L$ the flux vanishes. The glass and cells are impermeable.

3) Thermo-Viscoelastic Stress and Debond Driving Force

The in-plane mismatch strain of the encapsulant relative to the glass combines thermal contraction from the lamination temperature T_{lam} and hygroscopic swelling:

$$\varepsilon_m = \Delta\alpha\,(T - T_{lam}) + \alpha_H\,C \tag{3}$$

The encapsulant is a standard linear solid with an equilibrium modulus E_∞ and a relaxing branch E_1, whose relaxation time follows an Arrhenius law:

$$\sigma = E_\infty \varepsilon_m + q, \qquad \dot{q} = E_1\dot{\varepsilon}_m - \frac{q}{\tau(T)}, \qquad \tau = \tau_{85}\,\mathcal{A}(-E_v,T) \tag{4}$$

Relaxation is fast at 85 °C ($\tau_{85} = 1$ s) and effectively frozen near −40 °C, so cooling builds stress that the next hot dwell releases. Following thin-film fracture mechanics, the energy-release rate available for debonding at position x is

$$G(x,t) = \psi(x)^2\,\frac{h_f\,\sigma^2}{2E_{ref}}, \qquad \psi(x) = 1 + \kappa_e\,e^{-x/\ell_e} \tag{5}$$

where h_f is the thickness of the front encapsulant layer and ψ is a phenomenological stress-concentration factor of the frame-constrained edge, which decays over the length ℓ_e. For $\psi = 1$, Eq. (5) is the steady-state energy-release rate of a thin film debonding from a stiff substrate, $G = h_f\sigma^2/(2\bar{E})$ (Hutchinson & Suo, 1992). Because the film is viscoelastic, the plane-strain modulus $\bar{E}$ is replaced by a fixed effective modulus E_{ref} that lies between the relaxed ($E_\infty = 3$ MPa) and unrelaxed ($E_\infty + E_1 = 63$ MPa) values; Eq. (5) therefore estimates the driving force but is not an exact viscoelastic fracture solution. With σ in Pa and h_f in m, G is in J m^{-2}.

4) Interface Damage with Hydrolytic Weakening

The interface follows a bilinear cohesive law with a fixed ratio $r = \delta_f/\delta_0$ between the final and initiation openings. Equating the stored energy with $1/2\, k_0\delta^2$ gives the equivalent opening ratio $\delta/\delta_0 = \sqrt{rG/G_c}$, and the bilinear damage law with an irreversibility condition becomes

$$d_{mech}(x,t) = \max_{s\le t}\left\langle \frac{r\,(\delta/\delta_0 - 1)}{(\delta/\delta_0)(r-1)} \right\rangle_{[0,1]} \tag{6}$$

Damage initiates when $G > G_c/r$ and is complete when $G \ge rG_c$. This equivalent-opening mapping is an approximation: it does not track the softening branch of the traction–separation curve or a moving crack tip, and full separation requires $G = rG_c$ rather than $G = G_c$. The variable d is therefore a phenomenological damage index whose evolution is controlled jointly by G_c and r, not a Griffith crack-front position. The fracture energy decreases instantaneously with water activity and irreversibly through hydrolysis of interfacial bonds, consistent with the hydrolysis-controlled debonding observed at high humidity (Bosco et al., 2019; K. Liu et al., 2024; Novoa et al., 2016):

$$G_c = G_{c,dry}(1 - \omega_G a_w)[f_r + (1 - f_r)e^{-\mathcal{H}}], \qquad \dot{\mathcal{H}} = k_{H,85}\,\mathcal{A}(E_H, T)\,a_w^2 \tag{7}$$

where $\mathcal{H}$ is the hydrolytic damage of the interfacial bonds and f_r is the fraction of adhesion that resists hydrolysis.

5) Ionic Conduction, Interphase Conduits and Electrode Kinetics

By the Nernst–Einstein relation, ionic conductivity is proportional to the product of mobile-ion content and ion diffusivity. Motivated by this, and without resolving individual ionic species, the conductivity of the hydrated encapsulant is written in the empirical form

$$\sigma_e = \sigma_{85}\,\mathcal{A}(E_\sigma, T)[1 + \alpha_C a_w][1 + \beta_h \xi], \qquad \dot{\xi} = k_{h,85}\,\mathcal{A}(E_h, T)\,a_w(1 - \xi) \tag{8}$$

where α_C captures water plasticisation and ξ is the hydrolysed fraction of acetate groups, which releases mobile H^+/CH_3COO^- in EVA ($k_h = 0$ for POE); σ_e is in S m^{-1} and k_h in s^{-1}. The lateral transport is described by the sheet conductance $g(x,t)$ (in S) of the layered stack, i.e. the sum of conductivity × thickness over four parallel paths; a strip of length dx along the perimeter P then has the conductance $gP/\mathrm{d}x$:

$$g(x,t) = \underbrace{h_e\sigma_e}_{\text{bulk}} + \underbrace{h_I\sigma_e(1 + \alpha_d\, d)}_{\text{interphase conduit}} + \underbrace{h_g\sigma_g(T)}_{\text{glass}} + \underbrace{\sigma_w h_w(t)}_{\text{surface film}} \tag{9}$$

The conduit term is the core of the coupling. An intact interface ($d = 0$) adds only a negligible 20 μm of bulk-like polymer. A debonded interface ($d \to 1$) carries tangential transport amplified by $1 + \alpha_d$, which represents the ratio of ionic mobility in the water-filled gap to that in the crosslinked polymer. Ions in liquid water are typically several orders of magnitude more mobile than in a crosslinked polymer, so $\alpha_d = 10^3$ was chosen as a moderate, assumed value; it is not measured, and its influence is quantified in Section III.F. The glass conductivity σ_g is Arrhenius-activated. The surface term is active only when a condensate film of thickness h_w forms on the glass surface Γ_s:

$$\rho_w \dot{h}_w = h_{mt}\big[\rho_{v,\infty}(T_{air}, RH) - \rho_{v,sat}(T_s)\big], \qquad 0 \le h_w \le h_{w,max} \tag{10}$$

where ρ_w is the density of liquid water, ρ_v are water-vapour densities (kg m^{-3}) from the Magnus saturation pressure and the ideal-gas law, and the glass surface temperature T_s follows the air temperature as a first-order lag with time constant $\tau_s = 0.3$ h. Negative values of the bracket (evaporation) are allowed until $h_w = 0$; σ_w is the effective conductivity of the film.

The cells are equipotential at $V = 1000$ V, so the current through the edge region is $I = (V - \eta)/R_{lat}$, with the series resistance $R_{lat} = P^{-1} \int_0^{x_c} g^{-1}\, \mathrm{d}x$ in Ω (m divided by S·m). At the frame contact, the current is converted by Butler–Volmer kinetics on the electrochemically active area A_{act}:

$$I = A_{act}\, i_0 \left[e^{\alpha_a F\eta/R_g T} - e^{-\alpha_c F\eta/R_g T} \right] \tag{11}$$

$$A_{act} = P\, w_{el}\, \phi_0 \left(1 + \alpha_i \bar{d}_{el}\right), \qquad i_0 = i_{0,85}\, \mathcal{A}(E_i, T)\, \bar{a}_{w,el} \tag{12}$$

Here w_{el} is the width of the frame contact, ϕ_0 is its intact active fraction, and $\bar{d}_{el}$ and $\bar{a}_{w,el}$ are averages over the contact zone ($\bar{a}_{w,el}$ is floored at 10^{-3} to avoid a vanishing exchange current in dry conditions). i_0 is in A m^{-2}, $F\eta/R_gT$ is dimensionless, and η is counted positive in the direction that drives $I > 0$; because $\alpha_a = \alpha_c$, the kinetics are symmetric and this sign convention does not affect the result. Equations (11)–(12) and $I = (V - \eta)/R_{lat}$ are solved together for η at every step. Because R_{lat} dominates, η stays below 0.2 V in DH and below 0.64 V in every protocol, while the remaining ≈1000 V drop across the laminate. This corresponds to the thin-double-layer limit of the Poisson–Nernst–Planck equations for polymeric electrolytes, in which the bulk obeys Ohm's law and the interfaces are lumped (van Soestbergen et al., 2008). A single, lumped electrode reaction is assumed; the individual cathodic and anodic reactions are not resolved.

6) Corrosion–damage Feedback

The faradaic charge passed through the frame contact dissolves metal and generates hydroxide at the interface (Kempe et al., 2023; Li et al., 2018), which weakens the adhesion near the electrode. The total damage is

$$d = \min\left\{1,\ d_{mech} + \kappa_c\, \chi(x) \int_0^t \frac{I}{P\, w_{el}}\, \mathrm{d}s \right\}, \qquad \chi(x) = e^{-x/\ell_{el}} \tag{13}$$

where the charge density $\int I/(Pw_{el})\, \mathrm{d}s$ is in C m^{-2} and κ_c in m^2 C^{-1}, so that the added damage is dimensionless. Because $I > 0$ and d_{mech} is non-decreasing, d is non-decreasing. Higher current raises the damage, the damage raises the conductance through Eq. (9), and the conductance raises the current, closing the mechanics–electrochemistry loop. Fig. 2 summarises the architecture of the coupled model.

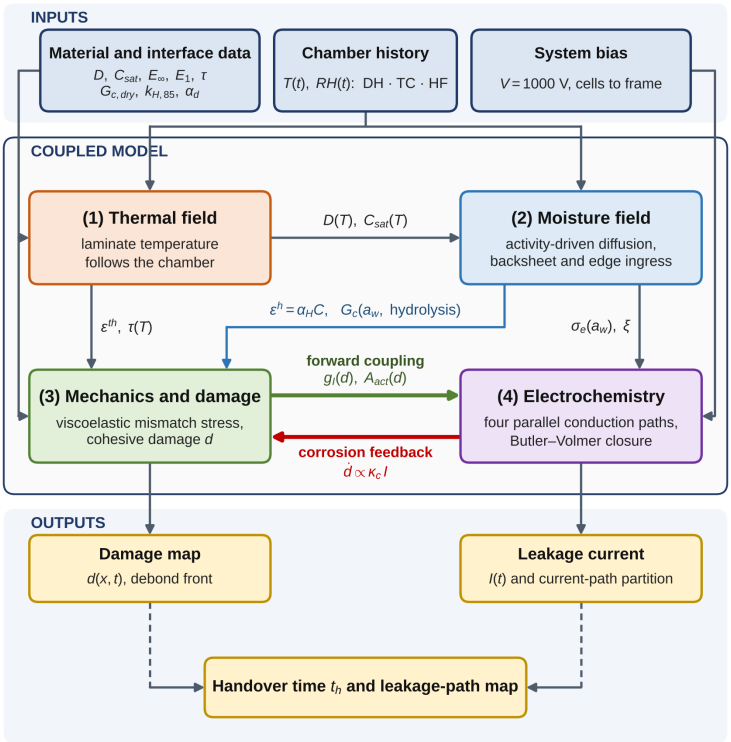


Fig. 2. Architecture of the coupled model. Material data, chamber history and bias (top) drive the four coupled fields (centre). The forward coupling (green) converts interface damage d into conduit conductance g_l and active electrode area A_{act}; the corrosion feedback (red) converts faradaic charge into further damage. The damage map, leakage current with its path partition, and the handover time t_h (bottom) are emergent outputs.

7) Thermodynamic Consistency Check

The reduced model is not derived from a free-energy functional, so its thermodynamic consistency cannot be proved here. A necessary check is nevertheless possible. Assuming mixing free energies for water and ions, the elastic energy $(1-d)W_e$ and a cohesive potential, the isothermal Clausius–Duhem inequality would reduce to the dissipation rate

$$\mathcal{D} = \int [M_m \parallel \nabla\mu_m \parallel^2 + \sum_k M_k \parallel \nabla\tilde{\mu}_k \parallel^2 + \mathcal{A}_h r_h]\mathrm{d}V + \int_{\Gamma_I} Y_I \dot{d}\, \mathrm{d}A + \int_{\Gamma^{el}} i_F\, \eta\, \mathrm{d}A \;\geq 0 \tag{14}$$

where M_m and M_k are mobilities, $\tilde{\mu}_k$ are electrochemical potentials, $\mathcal{A}_h r_h$ is the hydrolysis affinity–rate product, $Y_I \geq 0$ is the energy release conjugate to d, i_F is the faradaic current density and every term has units of W. The constitutive choices of Sections II.A.2–II.A.6 make each term non-negative:

- the mobilities are non-negative, including after any damage amplification;
- Eqs. (6) and (13) only increase d;
- hydrolysis proceeds along its affinity;
- Eq. (11) gives $\mathrm{sign}(i_F) = \mathrm{sign}(\eta)$.

The damage-amplified transport and the corrosion feedback therefore do not violate this necessary condition. The check constrains the signs of the couplings, not their magnitudes, and it is not a substitute for a full variational derivation.

8) Numerical Implementation

Equation (1) is discretised by finite volumes on 150 cells (Δx = 0.2 mm, aligned with w_{el} and x_c) and integrated implicitly with a Thomas solver. Equation (4) uses the exact exponential update for the relaxing branch. Equations (6)–(13) are updated explicitly within each step, and Eq. (11) is solved by bisection. The time step is 0.1 h for DH, 0.05 h for TC and 0.02 h for HF. Refining the grid to 0.1 and 0.05 mm changed the 1000 h DH current by less than 0.1%, and halving the time step changed it by less than 0.01%. The sensitivity and map studies use a 0.5 mm grid and a 0.25 h step, which shifts the reference result by 0.2%. The lamination history (cooling from 145 °C, then 24 h at 25 °C) is simulated first, so that each test starts from the frozen-in viscous stress. The implementation is written in Python, vectorised over parameter sets so that each sensitivity study runs as a single batch, and provided as Supplementary Data S1. Unless stated otherwise, the values reported in Sections III.A–III.D refer to the 0.2 mm reference grid; values from the 0.5 mm grid (Sections III.E–III.F) are marked as such.

B. Simulation Set-Up

1) Parameters

Table 1 lists every parameter used in the simulations. The set is representative, not fitted: no parameter was calibrated against a measured leakage-current or delamination curve, and the results must be read as predictions of the model under these assumptions, not as properties of a particular module. The basis of each group is stated in the table. Moisture-transport parameters are of the same order as those reported for EVA (Blom et al., 2025; Kempe, 2006). The adhesion, damage and conduit parameters are assumed; they were chosen so that, under DH, damage initiates only after hydrolytic weakening, consistent with the hydrolysis-controlled debonding reported at high humidity (Bosco et al., 2019; Novoa et al., 2016). The conductivity scale was set so that the terminal current of the 0.36 m^2 mini-module is of order 0.1–1 μA at 1000 V; this is an order-of-magnitude choice, not a calibration. The two least-constrained parameters, α_d and $k_{H,85}$, are included in the sensitivity analysis of Section III.F. Because no parameter is calibrated, the model is verified (grid and time-step convergence in Section II.A.8; dimensional and sign checks in Appendix A) but not yet validated. Its predictions are compared qualitatively with published observations in Section III.G, which also specifies the measurements required for a quantitative validation.

Table 1. Model parameters (EVA reference set; values at 85 °C where applicable). Basis: L, same order as published EVA data; A, assumed representative value; O, set to give the order of magnitude of the terminal current; G, geometry of the mini-module.

Group	Parameters	Basis
Geometry	$L = 30$ mm, $x_c = 10$ mm, $h_e = 0.9$ mm, $h_f = 0.45$ mm, $h_g = 3.2$ mm, $h_I = 20$ μm, $w_{el} = 2$ mm, $P = 2.4$ m	G (A for h_I)
Moisture	$D_{85} = 6.0 \times 10^{-10}$ m^2 s^{-1}, $E_D = 38$ kJ mol^{-1}, $\beta_c = 0.5$, $C_{s,85} = 5.5 \times 10^{-3}$, $E_s = 25$ kJ mol^{-1}	L (A for β_c)
Backsheet / edge	$k_{b,85} = 6 \times 10^{-9}$ m s^{-1}, $k_{s,85} = 4 \times 10^{-8}$ m s^{-1}, $E_b = 30$ kJ mol^{-1} (both)	A

Group	Parameters	Basis
Viscoelastic	$\Delta\alpha = 2.5 \times 10^{-4}$ K^{-1}, $\alpha_H = 0.25$, $E_\infty = 3$ MPa, $E_1 = 60$ MPa, $\tau_{85} = 1$ s, $E_v = 120$ kJ mol^{-1}, $T_{lam} = 145$ °C	A
Driving force	$E_{ref} = 20$ MPa, $\kappa_e = 3$, $\ell_e = 2.5$ mm	A
Adhesion	$G_{c,dry} = 1200$ J m^{-2}, $\omega_G = 0.6$, $r = 8$, $f_r = 3 \times 10^{-4}$, $k_{H,85} = 7 \times 10^{-6}$ s^{-1}, $E_H = 60$ kJ mol^{-1}, exponent of a_w = 2	A
Acetate hydrolysis	$k_{h,85} = 10^{-7}$ s^{-1}, $E_h = 70$ kJ mol^{-1}, $\beta_h = 0.5$	A
Conduction	$\sigma_{85} = 3 \times 10^{-11}$ S m^{-1}, $E_\sigma = 95$ kJ mol^{-1}, $\alpha_C = 30$, $\alpha_d = 10^3$, $\sigma_{g,85} = 10^{-10}$ S m^{-1}, $E_g =$ 80 kJ mol^{-1}	O (σ_{85}, $\sigma_{g,85}$); A
Electrode / feedback	$V = 1000$ V, $i_{0,85} = 10^{-2}$ A m^{-2}, $E_i = 40$ kJ mol^{-1}, $\alpha_a = \alpha_c = 0.5$, $\phi_0 = 10^{-3}$, $\alpha_i = 20$, $\kappa_c = 10^{-3}$ m^2 C^{-1}, $\ell_{el} = 1.5$ mm	A
Surface film	$h_{mt} = 0.01$ m s^{-1}, $\sigma_w = 2.5 \times 10^{-7}$ S m^{-1}, $h_{w,max} = 50$ µm, $\tau_s = 0.3$ h	A

2) Choice of Encapsulants

EVA and POE were chosen because they bracket the two chemistries that matter for this mechanism. EVA has been the standard encapsulant of crystalline-silicon modules for decades, so most published data on moisture ingress, adhesion loss and leakage current refer to it (Kempe, 2006; Luo et al., 2017; Novoa et al., 2016). Its vinyl-acetate groups hydrolyse to acetic acid, it absorbs comparatively much water, and its adhesion degrades hydrolytically; it therefore activates every branch of the model. POE has become the main alternative, particularly in glass/glass and bifacial modules, because it contains no hydrolysable acetate, absorbs far less water and resists PID (Luo et al., 2017; Spinella et al., 2022). Comparing the two isolates the chemical branch of the model acetate hydrolysis and adhesion hydrolysis while its mechanical and electrical structure stays unchanged. For POE, five parameters were changed relative to Table 1 - $C_{s,85} = 0.6 \times 10^{-3}$ (×0.11), $D_{85} = 4.0 \times 10^{-10}$ m^2 s^{-1} (×0.67), $\sigma_{85} = 5 \times 10^{-12}$ S m^{-1} (×0.17), $\alpha_C = 10$ (×0.33) and $k_{H,85} = 2.3 \times 10^{-6}$ s^{-1} (×0.33) — and acetate hydrolysis was switched off ($k_h = 0$); all other values, including the adhesion energy, were kept. These ratios are assumed contrasts that reflect the qualitative differences cited above; they are not measured POE properties. Other encapsulants, such as ionomers or silicones, lie between or beyond these two limits and are left for future work. The POE set therefore represents an idealised polymer class; the durability of commercial POE films also depends on their additive package (Sen et al., 2026), which is not modelled.

3) Virtual Test Protocols and Reference Models

Three IEC 61215-type protocols were simulated, each preceded by the lamination history: The HF test was extended beyond the 10 cycles of IEC 61215 to follow the damage to saturation; the predicted handover nevertheless falls within the first cycle, i.e., well inside the standard sequence.

- DH: 85 °C and 85% RH for 1000 h;
- TC: −40 to +85 °C at 100 K h−1 with 0.5 h dwells (3.5 h per cycle), 200 cycles, dry (5% RH);
- HF: 20 h at 85 °C and 85% RH, then a ramp to 40 °C (0.5 h dwell) and back, 24 h per cycle, 50 cycles.

To isolate each coupling, four nested models were run under identical inputs:

- M0: conductivity depends on temperature only;
- M1: conductivity depends on temperature and moisture, Eq. (8), without damage coupling ($\alpha_d = \kappa_c = 0$) the current state of the art;
- M2: damage-amplified conduits without corrosion feedback ($\kappa_c = 0$);
- M3: the full model.

The bulk-to-interface *handover time* t_h is defined as the first time at which the interphase conduit carries more than half of the current entering the frame-contact zone.

III. Results and Discussion

A. Moisture Uptake and the Adhesion Criterion under Damp Heat

Fig. 3(a) compares the three thermal histories. Under DH, moisture enters through the backsheet and the edge sealant (Fig. 3(b)). The water activity in the cell zone reaches 0.39 after 24 h, 0.79 after 100 h and 0.846 (99.5% of the chamber value) after 200 h. The edge is wetter than the interior during the first 100 h, after which the profile is almost uniform. Moisture uptake alone therefore cannot produce any change in current after about 200 h.

Fig. 3(c) shows why the simulated interface nevertheless fails later. The driving energy rG is concentrated at the frame-constrained edge, where it is about an order of magnitude higher than at $x = 10$ mm. The fracture energy, ≈590 J m^{-2} once the interface is wet, decays almost uniformly through hydrolysis, to 14 J m^{-2} at 250 h and 1.1 J m^{-2} at 400 h. The lamination stress produces only a small edge damage ($d \approx 0.02$–0.07) during the first 350 h. Rapid damage growth starts where G_c first falls below rG — at the edge, at about 355 h — and the debond front then advances inwards as G_c continues to fall. Because a fraction f_r of the adhesion is hydrolysis-resistant, the front stops where the edge concentration has decayed: the half-damage front ($d \geq 0.5$) reaches 1.8 mm at 500 h, 2.8 mm at 600 h and 3.4 mm at 1000 h. Partial damage ($d \geq 0.1$) extends to 7.2 mm.

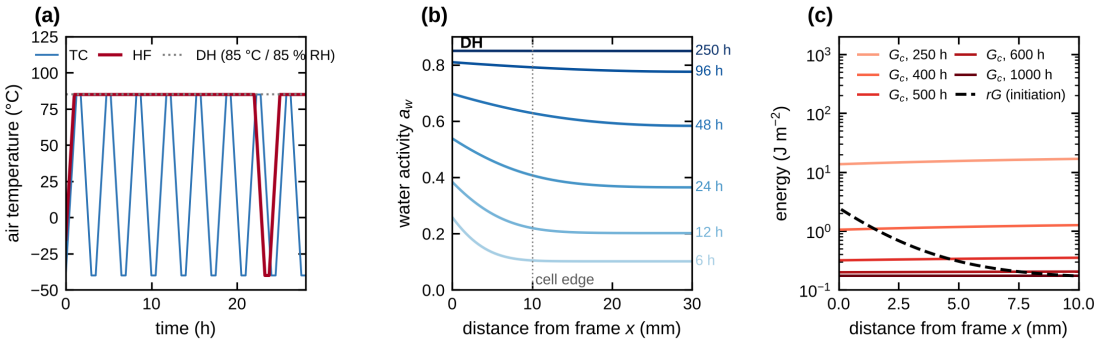


Fig. 3.(a) Air-temperature histories of the TC, HF and DH protocols. (b) Water activity in the encapsulant during DH. (c) Fracture energy $G_c(x)$ at successive DH times compared with the initiation threshold $rG(x)$; damage initiates where $G_c < rG$.

B. Leakage Current under Damp Heat: Four Nested Models

Fig. 4(a) and Table 2 compare the predictions of the four models.

- M0 (temperature-dependent conductivity) gives a constant 83 nA, set by the glass and dry polymer.
- M1 (moisture-dependent conductivity) rises to 256 nA at 200 h, tracking moisture uptake (steepest at 12 h), and then creeps to 275 nA through slow acetate hydrolysis. It has no late inflection: after 200 h its slope never exceeds 0.03 nA h−1.
- M3 (full model) follows M1 until about 350 h. It then shows a plateau, an accelerated-growth phase and saturation: the current rises from 314 nA at 400 h to 808 nA at 700 h (a factor of 2.6) and saturates at 908 nA. The inflection occurs at 592 h, with a slope of 2.46 nA h−1 about 80 times the largest post-200 h slope of M1.

In the model, this three-stage shape induction, acceleration and saturation, with the acceleration starting after moisture saturation is the electrical signature of interface debonding. A moisture-only model cannot produce it, because nothing in the moisture field changes after 200 h. M2, without corrosion feedback, reproduces the M3 trajectory to within 3.2% (879 nA at 1000 h, with $t_h = 430$ h), so in the model the acceleration is driven by the forward coupling. Fig. 4(b) shows the mechanism: the edge damage rises from 0.07 at 350 h to 0.82 at 500 h, and the conduit share of the current jumps from 0.26 at 420 h to above 0.8 at 456 h, around $t_h = 426$ h, long after the moisture activity has saturated.

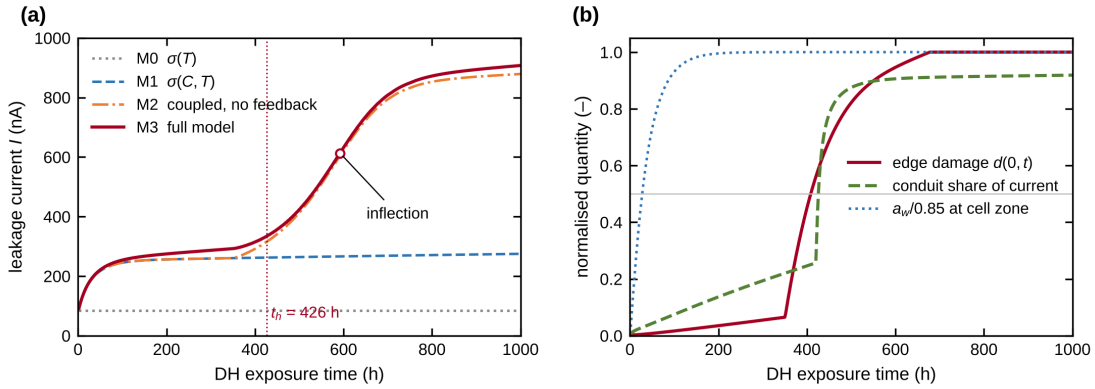


Fig. 4. Damp heat. (a) Leakage current predicted by the four nested models; the vertical line marks the handover time t_h of the full model and the circle its inflection point. (b) Edge damage $d(0,t)$, conduit share of the current entering the frame-contact zone, and normalised water activity $a_w/0.85$ in the cell zone for the full model.

Table 2. Damp-heat metrics of the nested models (EVA). I_{200} and I_{1000}: leakage current at 200 h and 1000 h; t_h: handover time (>1000: no handover within the test); inflection: time of maximum late-stage slope.

Model	I_{200} (nA)	I_{1000} (nA)	I_{1000}/I_{200}	t_h (h)	Inflection (h)
M0 $\sigma(T)$	83	83	1.00	>1000	none
M1 $\sigma(C,T)$	256	275	1.07	>1000	none
M2 coupled, no feedback	256	879	3.43	430	584
M3 full model	275	908	3.30	426	592

C. *Spatial Evolution and the Bulk-to-Interface Handover*

The damage profiles in Fig. 5(a) show the debond front starting at the frame contact and advancing inwards. They also show the step that the corrosion feedback adds inside the 2 mm contact zone, where the damage reaches 1.0 by 750 h. Fig. 5(b) partitions the current entering the contact zone among the three paths:

- at 200 h, the bulk encapsulant carries 60%, the glass 26% and the conduit 14%;
- at 1000 h, the conduit carries 92%, the bulk 6% and the glass 2%.

The handover is abrupt. The conduit conductance scales as $h_l \alpha_d d$, so once d exceeds about $h_e/(h_l \alpha_d) \approx 0.05$, the 20 µm interphase out-conducts the 0.9 mm bulk. The total current increases less steeply than the conduit share, because the undamaged inner part of the path (beyond ≈3–7 mm) remains in series. The terminal current therefore saturates once the front stops, even though the conduit dominates locally.

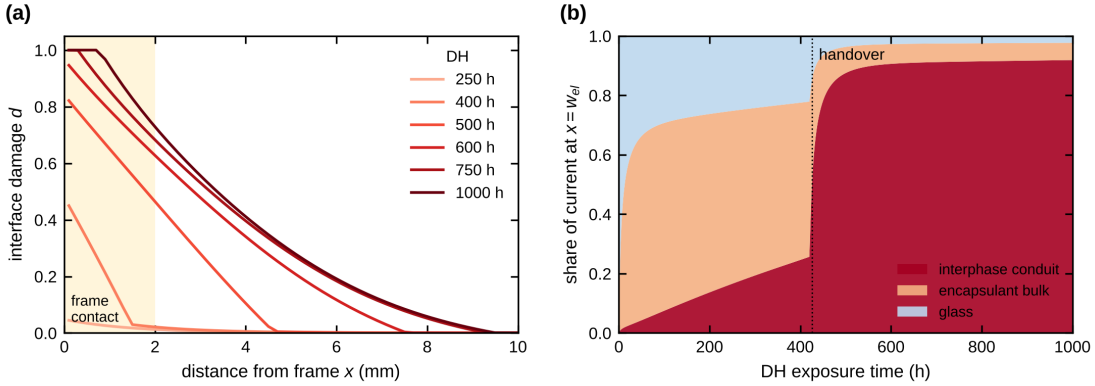


Fig. 5. Damp heat, full model. (a) Interface damage profiles $d(x)$; the shaded band is the frame-contact zone ($0 \le x \le w_{el}$). (b) Share of the current entering the contact zone at $x = w_{el}$ carried by the interphase conduit, the encapsulant bulk and the glass.

D. *Thermal Cycling and Humidity Freeze*

Thermal cycling. At −40 °C, relaxation is frozen, and the mismatch stress at the edge reaches 1.35 MPa. Cooling also lowers the water solubility (Eq. (2)) faster than the trace of water absorbed at 5% RH can leave, so the water

activity is capped at 1 in the cold phase and the instantaneous weakening term of Eq. (7) acts even in this dry test. The edge damage reaches 0.45 in the first cycle and 0.64 by cycle 10, and then barely grows (0.66 at cycle 200), because relaxation during each 85 °C dwell resets the stress and the hydrolytic loss of adhesion is negligible at 5% RH (Fig. 6(a)). Partial damage ($d \geq 0.1$) is confined to the outer 3.2 mm. Locally, the conduit share at the contact passes 0.5 after about eight cycles, but the conduits are dry and short: the hot-dwell current of M3 increases by only 32% (84 to 111 nA), mostly within the first 50 cycles, compared with 9% for M1. TC therefore exercises the mechanical branch without changing the terminal current appreciably. This TC result depends on the cold-phase supersaturation: with a temperature-independent solubility ($E_s = 0$) the edge damage stays at 0.34 and no handover occurs, and with $E_s = 12.5$ kJ mol^{-1} it reaches 0.43, again without handover (0.5 mm grid). Because the equilibrium assumption behind the cap probably overstates the effect of a trace of water, the TC damage should be regarded as an upper estimate.

Humidity freeze. HF combines the two branches. Each cold phase loads an interface that is wet and has been hydrolytically weakened during the preceding 20 h dwell. The edge damage reaches 0.66 after the first cycle, 0.84 after four cycles and 1.0 by cycle 7, and the whole 10 mm path is debonded by the end of the test. The handover occurs at $t_h = 21.8$ h, during the first cold phase about 20 times earlier than under DH. Unlike the TC result, this one is robust to the solubility assumption: t_h is 21.8 h for $E_s = 12.5$ kJ mol^{-1} and 47.7 h for $E_s = 0$. The wet-dwell current of M3 rises from 136 nA (cycle 1) to 3474 nA (cycle 11) and 4553 nA (cycle 50), a 33-fold increase; for M1 the increase is only from 135 to 274 nA (Fig. 6(b)).

The condensation-activated surface path produces thaw spikes lasting about 1.5 h, which reach 3.2–3.4 µA in both models in the first cycle. These are about 25 times the wet-dwell current in cycle 1, consistent in order of magnitude with the increase reported for wet outdoor conditions (Dhere et al., 2014b). As the conduits open, the spike-to-baseline ratio of M3 falls to 1.7. The surface path, which dominates the signal of an intact module, is thus masked in a delaminated one — a further reason why the terminal current alone is an ambiguous indicator. Resolving these spikes experimentally requires current readings at intervals of a few minutes, well below the spike duration.

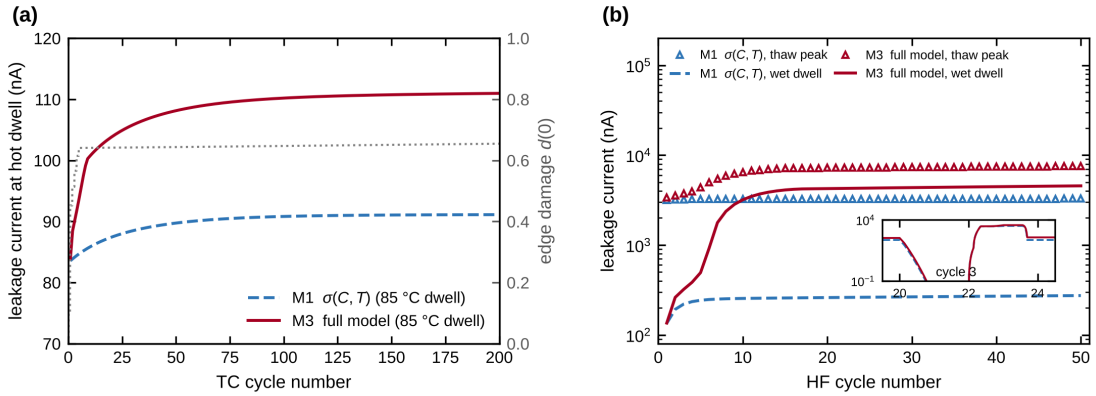


Fig. 6. (a) TC: leakage current at the 85 °C dwell of each cycle (left axis) and edge damage $d(0)$ of the full model (dotted, right axis). (b) HF: wet-dwell current (lines) and thaw-spike peak (triangles) per cycle; the inset shows the current through the thaw of cycle 3 on a logarithmic scale.

E. Encapsulant Chemistry and Climatic Acceleration

Replacing EVA with POE removes acetate hydrolysis and lowers the water solubility ninefold and the hydrolytic-weakening rate threefold. Under DH, the predicted POE current stays at 88–90 nA, the edge damage reaches only 0.21, and no handover occurs within 1000 h (Fig. 7(a)). Under HF, the cold-phase stresses still damage the POE edge, and the handover occurs at 116 h (cycle 5), five times later than for EVA; the edge is fully debonded only by cycle 16, and the wet-dwell current increases from 81 to 313 nA, compared with 136 to 4553 nA for EVA. In the model, POE therefore suppresses the mechanism under DH and delays and weakens it under HF, but does not prevent it. This is consistent with the qualitative ranking of POE above EVA in leakage-related durability (Luo et al., 2017; Spinella et al., 2022), and the model attributes the difference mainly to the adhesion-hydrolysis and solubility branches rather than to the bulk resistivity.

Fig. 7(b) maps the handover time under constant climates from 65 to 95 °C and 55 to 95% RH. t_h ranges from 230 h (95 °C, 95% RH) to 2925 h (65 °C, 55% RH), with 435 h at the standard 85 °C/85% RH (0.5 mm grid; 426 h on the reference grid). Excluding the one case close to the 3000 h simulation horizon, the 19 remaining points follow a Peck-type relation, $t_h \propto RH^{-n}\exp(E_a/R_gT)$, with $n = 1.94$, $E_a = 51$ kJ mol^{-1} (0.53 eV) and $R^2 = 0.9995$.

The relation has the same form as the temperature–humidity acceleration models used for PV degradation and combined-accelerated stress testing (Hacke et al., 2023). Within the model, the fit provides an explicit acceleration factor for the interface-mediated leakage mechanism, for instance 2.7 between 65 °C/85% RH and 85 °C/85% RH. Because the parameters are not calibrated, these values illustrate the form of the law, not its constants for a real encapsulant. Moreover, the fitted exponent n ≈ 2 and the activation energy of 51 kJ mol⁻¹ (compared with E_H = 60 kJ mol⁻¹) largely reflect the quadratic water-activity dependence and the Arrhenius activation of the hydrolysis rate in Eq. (7). The acceleration law is therefore a consequence of the constitutive choices rather than an independent result, and its constants must be determined experimentally.

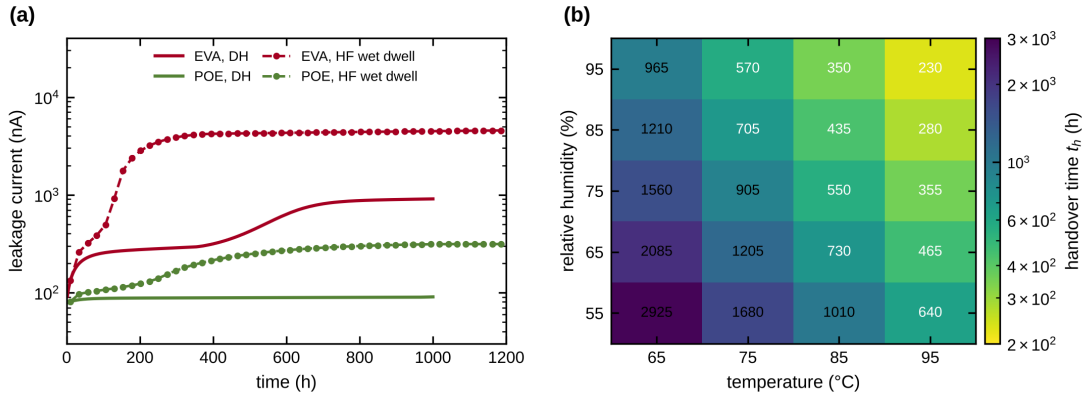


Fig. 7. (a) EVA versus POE: DH current (solid) and median wet-dwell current per HF cycle (dashed with markers). (b) Bulk-to-interface handover time t_h (h) under constant temperature and humidity (EVA, full model).

F. Sensitivity and Uncertainty

A Saltelli design with 512 base samples (4608 model runs, Jansen estimator for the total-order indices) varied seven parameters log-uniformly by a factor of two around the reference set (Fig. 8). The results separate the parameters into three groups:

- The adhesion and conduit parameters control the magnitude of the leakage current. The total-order indices for I(1000 h) are 0.59 for $G_{c,dry}$, 0.24 for α_d, 0.24 for σ_{85} and 0.07 for $k_{H,85}$. The first-order indices sum to 0.74, so about a quarter of the variance arises from interactions — as expected from the multiplicative coupling in Eq. (9).
- The hydrolysis rate alone controls the timing. The total-order index of $k_{H,85}$ for t_h is 0.98, with all other total-order indices below 0.1.
- The moisture diffusivity and the electrode parameters α_i and κ_c have little influence (total-order indices ≤ 0.06) within this range. Once the encapsulant saturates within about 200 h, moisture transport no longer limits the process, and the electrode overpotential is too small to matter.

Propagating the parameter ranges gives a 5–95% interval of 366–4170 nA for I(1000 h) (median 862 nA) and 260–760 h for t_h (median 435 h). The current is therefore uncertain by an order of magnitude, whereas the handover time is constrained to within a factor of three — an argument for using t_h, rather than the current magnitude, as a durability metric. The factor-of-two range is, however, narrow for the unmeasured amplification α_d. Because the damage level needed for handover scales as h_e/(h_I α_d) (Section III.C), a tenfold lower α_d would raise it from about 0.05 to about 0.45, making the handover time more dependent on the damage law; wider, order-of-magnitude ranges should be explored once measurements constrain α_d.

The corrosion feedback is weak at the reference value $\kappa_c = 10^{-3}$ m^2 C^{-1} but becomes decisive at higher values. Raising κ_c to 3×10^{-3}, 10^{-2} and 3×10^{-2} m^2 C^{-1} advances t_h from 430 h to 390, 130 and 50 h (0.5 mm grid, 5 h output interval) and increases I(1000 h) by 5%, 21% and 71%, respectively. Above roughly 10^{-2} m^2 C^{-1}, the loop becomes self-sustaining: the current-driven damage at the contact opens the conduit before hydrolysis does. This regime corresponds to the leakage-current-enhanced delamination observed under negative bias (Li et al., 2018).

Frontier Energy System and Power Engineering (FESPE)
Vol. 8, Issue 2, June 2026, pp. 53-68 e-ISSN: 2654-5667

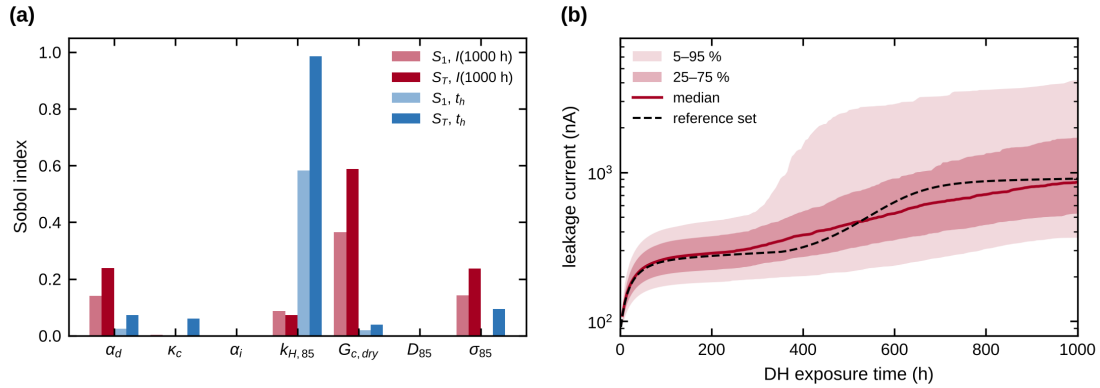


Fig. 8. (a) First-order (S_1) and total-order (S_T) Sobol indices for the 1000 h DH current and the handover time. (b) DH current: median, interquartile and 5–95% bands from 512 parameter samples, with the reference set.

G. *Discussion*

Implications for accelerated testing. If the model's mechanism holds, the simulations suggest three things that a terminal-current reading cannot reveal; each is a hypothesis to be tested experimentally:

1. A late acceleration of the DH current, occurring after moisture saturation, indicates interface debonding rather than a bulk transport non-linearity. A moisture-only model cannot reproduce it (Table 2).
2. TC and DH each exercise only one branch of the mechanism. In the simulations, HF combines stress with hydrolytic weakening and advanced the handover about twentyfold (Section III.D), so sequences that alternate wet exposure with cold cycling, such as combined-accelerated stress testing (Hacke et al., 2023; Owen-Bellini et al., 2021), are more discriminating for interface-mediated leakage.
3. Because the surface path dominates the current of an intact module and is masked in a delaminated one, the ratio of thaw-spike to wet-dwell current is itself a non-destructive indicator of conduit formation (Section III.D).

Durability metric. In the model, the handover time t_h is less uncertain than the current magnitude (5–95% interval 260–760 h; Section III.F), depends almost only on the adhesion-hydrolysis rate within the explored parameter range, and obeys a Peck relation (Section III.E). If these properties are confirmed experimentally, t_h could be estimated from DH tests at two climates and extrapolated to field conditions. Adhesion metrology on conditioned specimens (Bosco et al., 2019; Tracy et al., 2017) is the most valuable characterisation input, because $G_{c,dry}$ and $k_{H,85}$ dominate the variance.

Qualitative consistency with published observations. The predicted behaviour is consistent, in kind but not yet in magnitude, with independent observations:

- Moisture saturation of EVA behind a breathable backsheet within days at 85 °C (Blom et al., 2025; Kempe, 2006);
- edge-initiated delamination and its strong acceleration by temperature and humidity (Bosco et al., 2019; Novoa et al., 2016);
- an order-of-magnitude increase of the leakage current under wet conditions (Dhere et al., 2014b);
- the superior performance of POE encapsulants (Spinella et al., 2022).

These comparisons also delimit the contribution of the model. Path-resolved measurements (Dhere et al., 2014a, 2014b) showed that the dominant leakage path changes with surface wetness, but they could not attribute a rising bulk-path current to moisture uptake or to debonding; the present model proposes such an attribution. Finite-element and Poisson–Nernst–Planck models (Martinez-Loran et al., 2022; van Soestbergen et al., 2008) resolve the electric field and Na^+ transport in more detail than Eq. (8), but for a fixed material state; the results suggest that this assumption is adequate only before the handover. Conversely, the results qualify the common reading of POE as immune to interface-mediated leakage (Luo et al., 2017): under HF it delays rather than prevents the handover. Finally, the cohesive-zone models of PV laminates (Z. Liu et al., 2022) and the present reduced model agree that delamination initiates at the constrained edge, but the present model adds the electrical consequence of that initiation.

Status and limitations of the model. This is a computational study. The model has not been validated against measurements, and none of its predictions should be read as an experimental finding. Its limitations fall into three groups.

Parameters and validation.

- The parameter set is representative, not fitted (Table 1). The adhesion, damage, conduit and electrode parameters are assumed, and the two most influential ones, α_d and $k_{H,85}$, have no direct measurement. The predicted currents and times are therefore illustrative; the sensitivity analysis shows how far they can move.
- The agreement with published observations listed above is qualitative. No simulated curve has been compared with a measured leakage-current or delamination record from the same module.

Mathematical simplifications.

- The through-thickness averaging represents the debond front by a single interface and cannot distinguish the glass, cell and backsheet interfaces individually.
- The edge-concentration factor $\psi(x)$ and the effective modulus E_{ref} replace a resolved two-dimensional viscoelastic stress analysis; cell cracking under TC (Papargyri et al., 2020) is therefore not captured.
- The equivalent-opening damage law (Eq. (6)) is an approximation of a bilinear cohesive zone; d is a damage index, not a crack-front position.
- The thermodynamic argument of Section II.A.7 is a necessary-condition check, not a derivation of the reduced equations from a free energy.

Physical scope.

- The ionic conductivity is lumped (Eq. (8)), so individual ions, space charge and PID of the shunting and polarization types (Martinez-Loran et al., 2022; Yamaguchi et al., 2023) are outside the present scope.
- A single lumped electrode reaction is assumed, and the corrosion–damage law is linear in charge and does not represent passivation.
- The condensate film is spatially uniform, and UV-driven degradation, a growing concern for modern cell architectures (Khan et al., 2026), is not included. Only one bias polarity (cells at +1000 V relative to the frame) was simulated; negative bias, which drives Na^+ from the glass towards the cells and is the PID-relevant case (Arriaga Arruti et al., 2024; Luo et al., 2017; Yamaguchi et al., 2021), may produce a different response. The TC damage relies on equilibrium cold-phase supersaturation and should be regarded as an upper estimate (Section III.D).

Within the model, the leakage path hands over from the bulk to the interface when, and only when, the interface debonds. Whether real modules follow the same sequence, and on what time scale, has to be established experimentally for example, by path-resolved leakage measurements (Dhere et al., 2014a) combined with adhesion tests on humidity-conditioned specimens (Bosco et al., 2019; Tracy et al., 2017). A practical design would interrupt DH exposure of guard-ring-instrumented mini-modules at about 300, 400 and 500 h, bracketing the predicted handover, and pair each path-resolved current reading with peel or fracture tests on companion specimens.

IV. Conclusion

This study develops a reduced-order model of ionic conduction and interface degradation, identifying interface debonding as the key coupling mechanism between mechanical damage and leakage current. The uncalibrated model predicts that hydrolytic adhesion loss, rather than moisture uptake alone, drives late-stage leakage acceleration under damp heat, producing induction, acceleration, and saturation stages. Humidity freeze accelerates the transition from bulk to interfacial conduction through the combined effects of moisture and cyclic stress, whereas dry thermal cycling has limited impact. POE reduces degradation under damp heat and delays it under humidity freeze due to its lower moisture absorption and slower adhesion hydrolysis. Although the predicted handover time is more robust than the current magnitude, both remain illustrative because the model has not been calibrated or validated experimentally. These findings highlight the importance of humidity-conditioned adhesion measurements, combined-stress qualification tests, and hydrolytic adhesion stability in encapsulant selection. Future work will focus on experimental calibration, validation of moisture diffusion, and two-dimensional viscoelastic cohesive-zone modelling to improve predictive accuracy..

Author Contributions

All authors contributed equally to the conceptualization, data collection, data analysis, manuscript preparation, and revision of this article. All authors have read and approved the final version of the manuscript and agreed to be accountable for its content.

Funding

No funding support was received.

Declaration of Conflicting Interests

This section is compulsory. A competing interest exists when professional judgment concerning the validity of research is influenced by a secondary interest, such as financial gain. We require that our authors reveal any possible conflicts of interest in their submitted manuscripts. If there is no conflict of interest, the author should state that "The author (s) declare (s) that there is no conflict of interest regarding the publication of this paper". Some of the information you choose to provide here may constitute your “sensitive personal data”. (For example: All authors in this publication declare no conflict of interest regarding the title, data, location, and results of the research.).

Data Availability

A data availability statement is compulsory for research articles and clinical trials. Here, authors must describe how readers can access the data underlying the findings of the study, giving links to online repositories, and providing deposition codes where applicable. (For example: The datasets generated during and/or analysed during the current study are available from the corresponding author on reasonable request.).

Declaration on AI Use

Authors should declare any use of AI or AI-assisted technologies in their manuscripts, specifying the purpose, ensuring such use is limited to readability and language enhancement under human oversight, and. confirming that AI did not generate scientific insights, conclusions, or recommendations and is not credited as an author. The authors declare that no artificial intelligence (AI) or AI-assisted tools were used in the preparation of this manuscript. AI were used only to improve readability and language under strict human oversight; no content, ideas, analyses, or conclusions were generated by AI)

Appendix A. Dimensional and Sign Consistency of Eqs. (1)–(14)

Each equation was checked term by term for units and for the sign of its response, and the implementation in Supplementary Data S1 was checked against the equations line by line. Table A1 summarises the result. The check identified one sign error in an earlier version of the code, in which the Arrhenius factor of C_{sat} had the opposite sign to Eq. (2) and the solubility decreased with temperature. We corrected it, and recomputed all results in this paper with the corrected code.

Table A1. Units and sign checks of Eqs. (1)–(14); a dash denotes a dimensionless quantity.

Eq.	Quantity and units	Sign / monotonicity check
(1)	$\partial C/\partial t$, $\partial_x(D\,\partial_x C)$, $(k_b/h_e)(C_{sat}RH - C)$: all s^{-1}	Source vanishes at $C = C_{sat}RH$; $D > 0$
(2)	D [$m^2\ s^{-1}$]; C_{sat}, a_w, $\mathcal{A}$ [–]	$\partial C_{sat}/\partial T > 0$ for $E_s > 0$; D increases with T and a_w
(3)	ε_m [–]: $\Delta\alpha$ [K^{-1}] × K; α_H [–] × C [–]	Cooling below T_{lam} gives $\varepsilon_m < 0$; swelling reduces $\lvert\varepsilon_m\rvert$
(4)	σ, q [Pa]; $\dot{q}$ [Pa s^{-1}]; τ [s]	τ increases on cooling ($\mathcal{A}(-E_v, T)$)
(5)	G [J m^{-2}] = m × Pa^2 / Pa	$G \geq 0$; depends on σ^2, so independent of the sign of σ
(6)	δ/δ_0, d_{mech} [–]	$d_{mech} \in [0,1]$, non-decreasing
(7)	G_c [J m^{-2}]; $\mathcal{H}$ [–]; k_H [s^{-1}]	$G_c > 0$ since $\omega_G < 1$ and $f_r > 0$; $\dot{\mathcal{H}} \geq 0$
(8)	σ_e [S m^{-1}]; ξ [–]; k_h [s^{-1}]	$\sigma_e > 0$; $\xi \in [0,1)$, non-decreasing
(9)	g [S] = (S m^{-1}) × m; R_{lat} [Ω]	Each path ≥ 0; g non-decreasing in d
(10)	$\rho_w \dot{h}_w$ [kg $m^{-2}\ s^{-1}$] = (m s^{-1}) × (kg m^{-3})	Film grows only when $\rho_{v,\infty} > \rho_{v,sat}(T_s)$; $0 \leq h_w \leq h_{w,max}$
(11)	I [A] = m^2 × A m^{-2}; $F\eta/R_gT$ [–]	$\mathrm{sign}(I) = \mathrm{sign}(\eta)$; unique root $0 < \eta < V$
(12)	A_{act} [m^2]; i_0 [A m^{-2}]	A_{act} non-decreasing in $\bar{d}_{el}$
(13)	κ_c [$m^2\ C^{-1}$] × charge density [C m^{-2}] = [–]	d non-decreasing, capped at 1
(14)	Each integral [W]	Each term ≥ 0 under the stated constitutive choices

References

Arriaga Arruti, O., Gnocchi, L., Jeangros, Q., Ballif, C., & Virtuani, A. (2024). Potential-induced degradation in bifacial silicon heterojunction solar modules: Insights and mitigation strategies. *Progress in Photovoltaics: Research and Applications, 32*, 304–316. https://doi.org/10.1002/pip.3765

Ballif, C., Haug, F.-J., Boccard, M., Verlinden, P. J., & Hahn, G. (2022). Status and perspectives of crystalline-silicon photovoltaics in research and industry. *Nature Reviews Materials, 7*, 597–616. https://doi.org/10.1038/s41578-022-00423-2

Blom, Y., Jimenez Pelarda, D., Minett, T., Kaaya, I., Kyranaki, N., Santbergen, R., Isabella, O., & Vogt, M. R. (2025). Modeling moisture ingress in PV modules with different encapsulant and backsheet materials. *Renewable Energy, 252*, Article 123347. https://doi.org/10.1016/j.renene.2025.123347

Bosco, N., Tracy, J., & Dauskardt, R. (2019). Environmental influence on module delamination rate. *IEEE Journal of Photovoltaics, 9*, 469–475. https://doi.org/10.1109/JPHOTOV.2018.2877436

del Cueto, J. A., & McMahon, T. J. (2002). Analysis of leakage currents in photovoltaic modules under high-voltage bias in the field. *Progress in Photovoltaics: Research and Applications, 10*, 15–28. https://doi.org/10.1002/pip.401

Dhere, N. G., Shiradkar, N. S., & Schneller, E. (2014a). Device for detailed analysis of leakage current paths in photovoltaic modules under high voltage bias. *Applied Physics Letters, 104*, Article 112103. https://doi.org/10.1063/1.4869028

Dhere, N. G., Shiradkar, N. S., & Schneller, E. (2014b). Evolution of leakage current paths in MC-Si PV modules from leading manufacturers undergoing high-voltage bias testing. *IEEE Journal of Photovoltaics, 4*, 654–658. https://doi.org/10.1109/JPHOTOV.2013.2294764

Fu, J., Sen, C., Wang, H., Khan, M. U., Song, H., Lv, R., Huang, T., & Hoex, B. (2026). Assessing the impact of solder flux-induced corrosion on TOPCon solar cells. *Solar Energy Materials and Solar Cells, 294*, Article 113890. https://doi.org/10.1016/j.solmat.2025.113890

Hacke, P., Owen-Bellini, M., Kempe, M. D., Sulas-Kern, D. B., Miller, D. C., Jankovec, M., Mitterhofer, S., Topič, M., Spataru, S., Gambogi, W., & Tanahashi, T. (2023). Acceleration factors for combined-accelerated stress testing of photovoltaic modules. *Solar RRL, 7*, Article 2300068. https://doi.org/10.1002/solr.202300068

Hutchinson, J. W., & Suo, Z. (1992). Mixed mode cracking in layered materials. *Advances in Applied Mechanics, 29*, 63–191. https://doi.org/10.1016/S0065-2156(08)70164-9

Jordan, D. C., Kurtz, S. R., VanSant, K., & Newmiller, J. (2016). Compendium of photovoltaic degradation rates. *Progress in Photovoltaics: Research and Applications, 24*, 978–989. https://doi.org/10.1002/pip.2744

Kempe, M. D. (2006). Modeling of rates of moisture ingress into photovoltaic modules. *Solar Energy Materials and Solar Cells, 90*, 2720–2738. https://doi.org/10.1016/j.solmat.2006.04.002

Kempe, M., Hacke, P., Morse, J., Li, J., Shen, Y.-C., & Han, K. (2023). Electrochemical mechanisms of leakage-current in photovoltaic modules. *Progress in Photovoltaics: Research and Applications, 31*, 700–715. https://doi.org/10.1002/pip.3677

Khan, M. U., Ciesla, A., Johns, A., Sen, C., Huang, T., Song, H., Gao, M., Lv, R., Yu, Y., Wu, X., Wang, H., Wang, X., & Hoex, B. (2026). Charge trapping, hydrogen accumulation, and structural rearrangement: A complete model for ultraviolet-induced degradation in TOPCon devices. *Solar Energy Materials and Solar Cells, 298*, Article 114149. https://doi.org/10.1016/j.solmat.2025.114149

Li, J., Shen, Y.-C., Hacke, P., & Kempe, M. (2018). Electrochemical mechanisms of leakage-current-enhanced delamination and corrosion in Si photovoltaic modules. *Solar Energy Materials and Solar Cells, 188*, 273–279. https://doi.org/10.1016/j.solmat.2018.09.010

Liu, K., Thornton, P., D'hooge, D. R., & Dauskardt, R. H. (2024). Predicting encapsulant delamination in photovoltaic modules bridging photochemical reaction kinetics and fracture mechanics. *Progress in Photovoltaics: Research and Applications, 32*, 317–329. https://doi.org/10.1002/pip.3771

Liu, Z., Reinoso, J., & Paggi, M. (2022). Hygro-thermo-mechanical modeling of thin-walled photovoltaic laminates with polymeric interfaces. *Journal of the Mechanics and Physics of Solids, 169*, Article 105056. https://doi.org/10.1016/j.jmps.2022.105056

Luo, W., Khoo, Y. S., Hacke, P., Naumann, V., Lausch, D., Harvey, S. P., Singh, J. P., Chai, J., Wang, Y., Aberle, A. G., & Ramakrishna, S. (2017). Potential-induced degradation in photovoltaic modules: A critical review. *Energy & Environmental Science, 10*, 43–68. https://doi.org/10.1039/C6EE02271E

Martinez-Loran, E., von Gastrow, G., Clenney, J., Meier, R., Bandaru, P., Bertoni, M., & Fenning, D. (2022). Finite element simulation of potential-induced degradation kinetics in p-type silicon solar modules. *IEEE Journal of Photovoltaics, 12*, 45–52. [DOI?]

Mitterhofer, S., Slapšak, J., Astigarraga, A., Moser, D., Oviedo Hernandez, G., Chiantore, P. V., Luo, W., Khoo, Y. S., Rabanal-Arabach, J., Fuentealba, E., Ferrada, P., Trigo Gonzalez, M., Ascencio-Vásquez, J., Topič, M., & Jankovec, M. (2024). Measurement and simulation of moisture ingress in PV modules in various climates. *IEEE Journal of Photovoltaics, 14*, 140–148. https://doi.org/10.1109/JPHOTOV.2023.3323808

Novoa, F. D., Miller, D. C., & Dauskardt, R. H. (2016). Adhesion and debonding kinetics of photovoltaic encapsulation in moist environments. *Progress in Photovoltaics: Research and Applications, 24*, 183–194. https://doi.org/10.1002/pip.2657

Owen-Bellini, M., Hacke, P., Miller, D. C., Kempe, M. D., Spataru, S., Tanahashi, T., Mitterhofer, S., Jankovec, M., & Topič, M. (2021). Advancing reliability assessments of photovoltaic modules and materials using combined-accelerated stress testing. *Progress in Photovoltaics: Research and Applications, 29*, 64–82. https://doi.org/10.1002/pip.3342

Papargyri, L., Theristis, M., Kubicek, B., Krametz, T., Mayr, C., Papanastasiou, P., & Georghiou, G. E. (2020). Modelling and experimental investigations of microcracks in crystalline silicon photovoltaics: A review. *Renewable Energy, 145*, 2387–2408. https://doi.org/10.1016/j.renene.2019.07.138

Segbefia, O. K., Imenes, A. G., & Sætre, T. O. (2021). Moisture ingress in photovoltaic modules: A review. *Solar Energy, 224*, 889–906. https://doi.org/10.1016/j.solener.2021.06.055

Semba, T. (2020). Corrosion mechanism analysis of the front-side metallization of a crystalline silicon PV module by a high-temperature and high-humidity test. *Japanese Journal of Applied Physics, 59*, Article 054001. https://doi.org/10.35848/1347-4065/ab8274

Sen, C., Wang, H., Heidrich, R., Lüdemann, M., Khan, M. U., & Hoex, B. (2026). The dark side of certain POE encapsulant: Chemical pathways to metallisation corrosion in TOPCon modules. *Solar Energy Materials and Solar Cells, 298*, Article 114164. https://doi.org/10.1016/j.solmat.2026.114164

Sen, C., Wang, H., Khan, M. U., Fu, J., Wu, X., Wang, X., & Hoex, B. (2024). Buyer aware: Three new failure modes in TOPCon modules absent from PERC technology. *Solar Energy Materials and Solar Cells, 272*, Article 112877. https://doi.org/10.1016/j.solmat.2024.112877

Spinella, L., Uličná, S., Sinha, A., Sulas-Kern, D. B., Owen-Bellini, M., Johnston, S., & Schelhas, L. T. (2022). Chemical and mechanical interfacial degradation in bifacial glass/glass and glass/transparent backsheet photovoltaic modules. *Progress in Photovoltaics: Research and Applications, 30*, 1423–1432. https://doi.org/10.1002/pip.3602

Tracy, J., Bosco, N., Novoa, F., & Dauskardt, R. (2017). Encapsulation and backsheet adhesion metrology for photovoltaic modules. *Progress in Photovoltaics: Research and Applications, 25*, 87–96. https://doi.org/10.1002/pip.2817

Tsanakas, J. A., Babics, M., Mezzasalma, F., Mignonac, A., Colin, H., Sicot, L., Marechal, P., Capron, G., Rakotoniaina, J.-P., & Aimé, J. (2026). Long-term field degradation of crystalline-silicon PV modules: Insights from fifteen years of monitoring and forensic analysis. *EPJ Photovoltaics, 17*, Article 14. https://doi.org/10.1051/epjpv/2026006

van Soestbergen, M., Biesheuvel, P. M., Rongen, R. T. H., Ernst, L. J., & Zhang, G. Q. (2008). Modified Poisson–Nernst–Planck theory for ion transport in polymeric electrolytes. *Journal of Electrostatics, 66*, 567–573. https://doi.org/10.1016/j.elstat.2008.06.005

Wang, H., Sen, C., Khan, M. U., Huang, T., Song, H., Gao, M., Lv, R., Yu, Y., & Hoex, B. (2026). A novel damp heat-induced failure mechanism in PV modules (with case study in TOPCon). *Solar Energy Materials and Solar Cells, 299*, Article 114195. https://doi.org/10.1016/j.solmat.2026.114195

Weitsman, Y. (1987). Coupled damage and moisture-transport in fiber-reinforced, polymeric composites. *International Journal of Solids and Structures, 23*, 1003–1025. https://doi.org/10.1016/0020-7683(87)90093-X

Yamaguchi, S., Masuda, A., Marumoto, K., & Ohdaira, K. (2023). Mechanistic understanding of polarization-type potential-induced degradation in crystalline-silicon photovoltaic cell modules. *Advanced Energy and Sustainability Research, 4*, Article 2200167. https://doi.org/10.1002/aesr.202200167

Yamaguchi, S., Van Aken, B. B., Masuda, A., & Ohdaira, K. (2021). Potential-induced degradation in high-efficiency n-type crystalline-silicon photovoltaic modules: A literature review. *Solar RRL, 5*, Article 2100708. https://doi.org/10.1002/solr.202100708